nature photonics

SUPPLEMENTARY INFORMATION

DOI: 10.1038/NPHOTON.2013.214

Supplementary Information

Realization of an all-dielectric zero-index optical metamaterial

Parikshit Moitra[1†], Yuanmu Yang[1†], Zachary Anderson[2], Ivan I. Kravchenko[3], Dayrl P. Briggs[3], Jason Valentine[4]

[1]Interdisciplinary Materials Science Program, Vanderbilt University, Nashville, Tennessee 37212, USA
[2]School for Science and Math at Vanderbilt, Nashville, TN 37232, USA
[3]Center for Nanophase Materials Sciences, Oak Ridge National Laboratory, Oak Ridge, Tennessee 37831, USA
[4]Department of Mechanical Engineering, Vanderbilt University, Nashville, Tennessee 37212, USA

S1. Modeling and Homogenization

a. Retrieval of the effective index from the Bloch modes

Retrieval of the permittivity and permeability was carried out by extracting the average field components from the TM Bloch modes at the boundary of the unit cell $(\bar{E}_x, \bar{D}_x, \bar{H}_y, \bar{B}_y, \bar{H}_z, \bar{B}_z)$. In the extraction of the permittivity and permeability, we ensure the continuity of the tangential and normal components of the average field at the unit cell boundary, ensuring that Maxwell's equations are satisfied. The constitutive equations for the average fields are then given by,

$$\begin{bmatrix} \bar{D}_x \\ \bar{B}_y \\ \bar{B}_z \end{bmatrix} = \begin{bmatrix} \varepsilon_0 * \varepsilon_x & A_{xy} & A_{xz} \\ A_{yx} & \mu_0 * \mu_y & A_{yz} \\ A_{zx} & A_{zy} & \mu_0 * \mu_z \end{bmatrix} \begin{bmatrix} \bar{E}_x \\ \bar{H}_y \\ \bar{H}_z \end{bmatrix} \quad (1)$$

The diagonal elements of the 3 x 3 parameter tensor define the permittivity (ε_x) and permeability (μ_y, μ_z) of the bulk structure along the x, y and z directions respectively.

DOI: 10.1038/NPHOTON.2013.214

b. Optical property retrieval from the Bloch modes and extended states

To ensure that an accurate retrieval of the material properties was acquired, we compared the retrieved wavevector, computed with the retrieved effective index, to the band structure calculated numerically using MIT Photonic Bands (MPB) in the range from Γ to X, as illustrated in Fig. S1a. The retrieved band structure has a very good agreement with the MPB band structure at smaller k_y, though it deviates at large k_y as spatial dispersion becomes apparent near the band edge. Only the transverse bands are considered in the calculation of the effective optical properties.

In order to properly assign a refractive index to a material for off-normal angles of incidence, there must be only one propagating band at a particular frequency, the presence of only the fundamental mode, and a nearly circular isofrequency contour[1]. To verify that there is only one propagating band within the material, we simulated the extended states of the crystal, shown in Fig. S1b. Within the frequency range from 215 THz to 225 THz, slightly above the zero-index point, there is a single band (TM4) throughout *k*-space and nearly circular isofrequency contours as illustrated in Fig. 2c. Given the periodicity of the structure (600 nm) and the square lattice, higher order diffraction is prevented for wavelengths greater than 1200 nm. Furthermore, as mentioned in the text and as illustrated below in Fig. S5, the response of the structure is due to the linear combination of electric monopole and magnetic dipole resonances, further supporting homogenization of the material[2] within the frequency region from 215 THz to 225 THz. In the sections below we provide further evidence of this statement with full-wave simulations of the material.

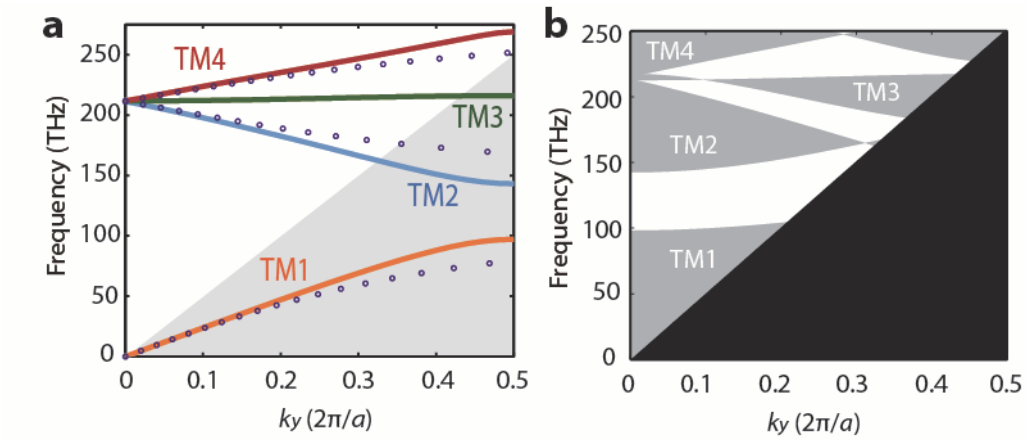

Figure S1 Comparison of optical properties and band structure and extended states of the metamaterial. a, The solid lines represent the band structure of the square lattice calculated from MPB and the circles correspond to band diagram retrieved from effective index n_{eff} and the dispersion relation $k_y = n_{eff}\,\omega/c$. The mismatch of the two methods at the band edge is due to the fact that the effective medium approximation no longer holds in those regions. **b,** Extended states of the crystal showing that only one band (TM4) is present between 215 THz and 225 THz, allowing an effective index to be assigned to this region.

c. Comparison of normal and angle dependent transmission between the ZIM and a homogeneous medium

To further verify the use of effective constitutive properties in the case of the ZIM, we also simulated normal and angle dependent transmission of a homogeneous medium with the same effective optical properties. The ZIM structure that was simulated consisted of 5 identical unit cells along the light propagation direction and the homogenous medium it was compared to was modeled with the optical properties acquired from the bulk metamaterial retrieval (Fig. 2b). In Fig. S2a and S2c, we compare the transmittance at normal incidence for the effective medium and ZIM, respectively. Transmittance for both cases stays near unity over the wavelength range of 1200 nm to 1600 nm, with some undulation in transmission occurring in the case of the ZIM. This undulation can be attributed to the limited thickness of the material and thus the optical properties have not fully converged to the bulk case. In Fig. S2b and S2d, the transmittance with respect to angle of incidence is plotted for the homogenous medium and the ZIM at wavelengths

DOI: 10.1038/NPHOTON.2013.214

of 1340 nm (n = 0.254) and 1380 nm (n = 0.121). These wavelengths lie within the frequency region where only a single band (TM4) exists. The close match between the results supports the assignment of effective optical properties to the ZIM.

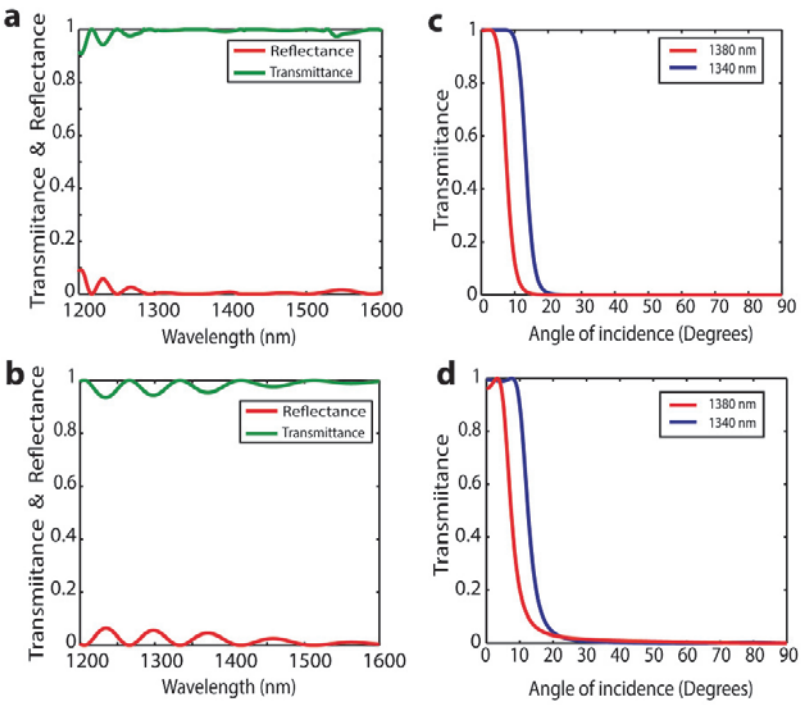

Figure S2 Comparison of normal and angle dependent transmittance of a homogeneous medium and the ZIM structure. a,c, Transmittance of the homogeneous medium and ZIM structure (5 periods), respectively, under normal incidence. **b,d,** Angle dependent transmittance of the homogeneous medium and ZIM structure, respectively, at wavelengths of 1340 nm and 1380 nm.

d. Beam propagation within the metamaterial

To further justify the claim that the proposed metamaterial structure can indeed be homogenized and has an isotropic low-index for TM-polarized light, we conducted numerical simulations of a Gaussian beam being incident on the ZIM at multiple angles. The wavelengths

of the incident beams (1340nm and 1380nm) are chosen such that they fall within the bandwidth where only one propagating band (TM4) exists.

The simulated electric field profiles are shown in Figs. S3 a-f. In all cases, we see no higher order diffraction taking place within the material. The transmitted light from the material is a Gaussian wave as shown in Figs. S3a,b,d,e for both normal and low-angle of incidence, while light transmission is clearly forbidden at higher angles due to the conservation of parallel angular momentum (Figs. S3c,f).

From the field plots in Fig. S3b, with 10° incidence at 1340 nm, the light refracts at an angle of ~ 43°. From Snell's law we find the corresponding n_{eff} is 0.255, agreeing with the retrieved index of 0.254. At 1380 nm, with a 5° incident angle, the refraction angle is ~ 46°, which corresponds to a n_{eff} of 0.121, again matching the parameter retrieval.

In Figs.S3g-i, we have simulated transmission at 1458 nm which is within the negative index region where the calculated index is -0.121. At normal incidence, the light transmits with a Gaussian profile and at 5° incidence we can clearly observe negative refraction inside the medium, and Snell's law is in agreement with the parameter retrieval. However, contrary to the single mode propagation at 1380 nm, transmission is not forbidden at a 30º angle of incidence for 1458 nm due to coupling to the quasi-longitudinal band. This illustrates why the metamaterial cannot be modeled as a homogenous medium for all-angles of incidence within the negative index region.

DOI: 10.1038/NPHOTON.2013.214

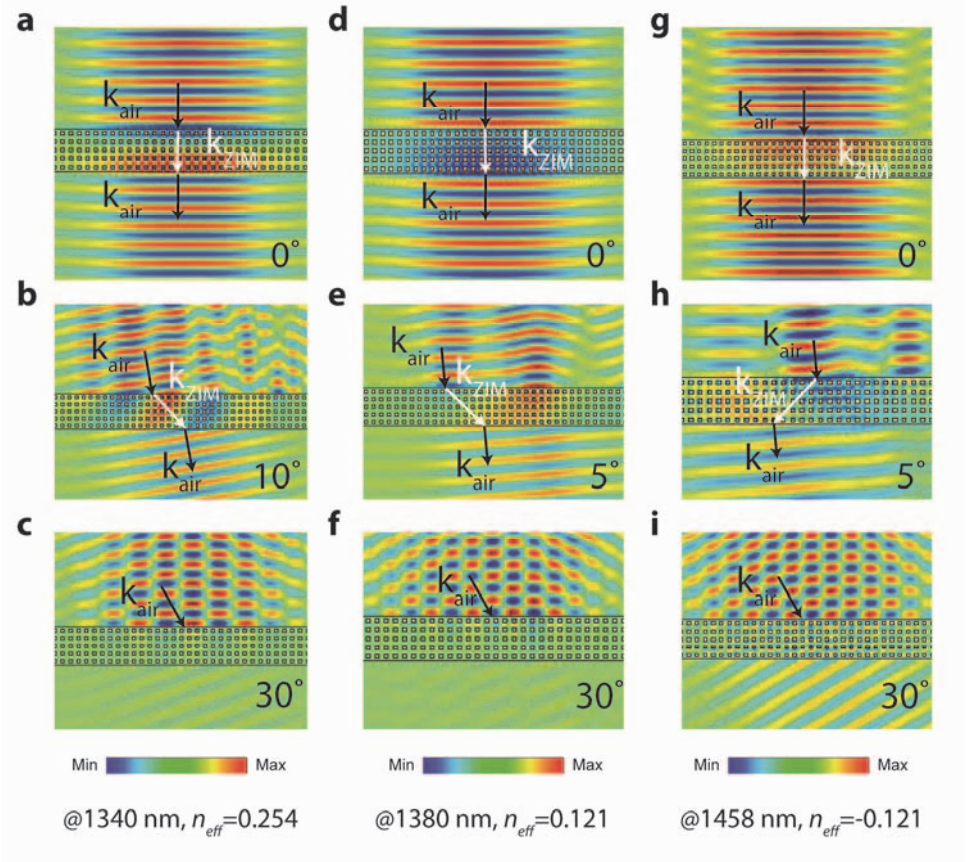

Figure S3 Simulated electric field plot of a periodic 5 layered ZIM probed with a Gaussian beam. a-c, Light incident at 0°, 10°, 30°, respectively, at a wavelength of 1340 nm. **d-f,** Light incident at 0°, 5°, 20°, respectively, at a wavelength of 1380 nm. **g-i**, Light incident at 0°, 5°, 20°, respectively, at a wavelength of 1458 nm.

e. Comparison of dispersion relation and effective optical properties as a function of Si rod filling fraction

We compared the dispersion relations and corresponding effective optical properties of the bulk ZIM as a function of the Si filling fraction to identify changes that could arise due to fabrication imperfections. Figures S4a,S4c show the band diagram with the Si filling fraction set at smaller (0.400) and larger (0.500) values than the zero-index case (0.433, Fig. S4b). With deviated filling fraction, the triple-degeneracy at the Γ point breaks up and the dispersion of two transverse bands changes from linear to quadratic. A bandgap opens between the two transverse

modes, leading to a discontinuity in the effective optical properties as well as impedance mismatch at the band edge, as shown in Fig. S4d and Fig. S4f. A similar effect is present in the fabricated structure due to non-uniform Si rod size.

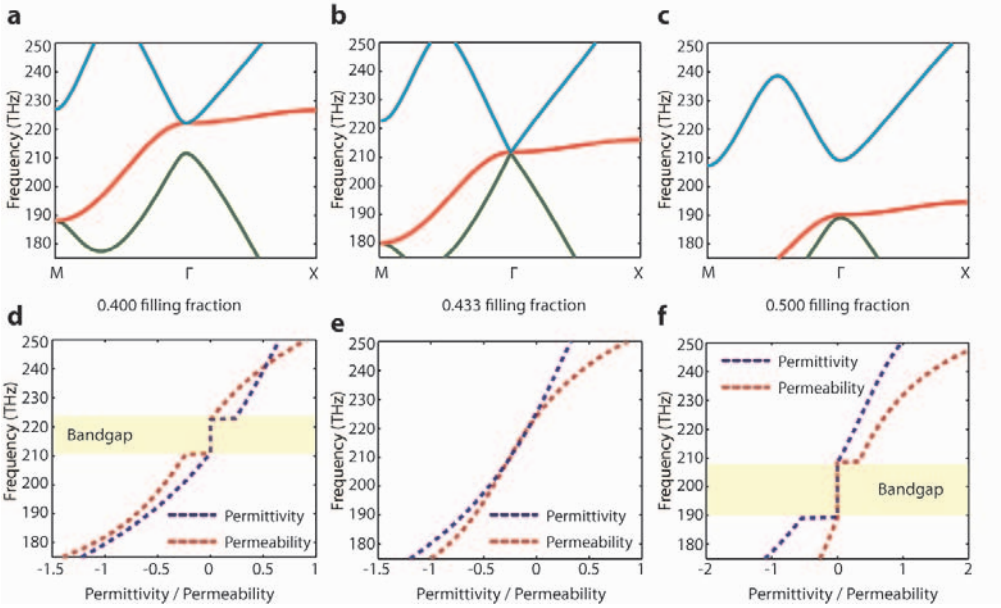

Figure S4 Band diagram and parameter retrieval for three different filling fractions. a-c, Band diagram of a square lattice with Si filling fraction of, **a** 0.400, **b** 0.433, **c** 0.500. The lattice constant is 600 nm, with $\varepsilon_{Si} = 13.7$, $\varepsilon_{SiO_2} = 2.25$. **d-f,** Corresponding retrieved optical properties of the bulk material using field averaging. A bandgap appears when the Si filling fraction deviates from the ideal design. In this case, at the band edge where index is low, the permittivity and permeability no longer match each other, leading to impedance mismatch to free space.

f. Field profile at zero-index point

Here, we show the electric and magnetic field profiles at a frequency that is slightly above the zero-index frequency ($f = 212\,THz$), where both the index of refraction and magnitude of the wavevector are close to zero. This leads to negligible spatial phase change across the length of the ZIM ($\varphi = kL$), where L is total thickness of the ZIM structure. In the field plots (Fig. S5), it is clear that the transmitted light leaves the ZIM / air interface with the same phase as the

DOI: 10.1038/NPHOTON.2013.214

incident plane wave. The unit cells also show strong electric and magnetic resonances, which are resonating in-phase.

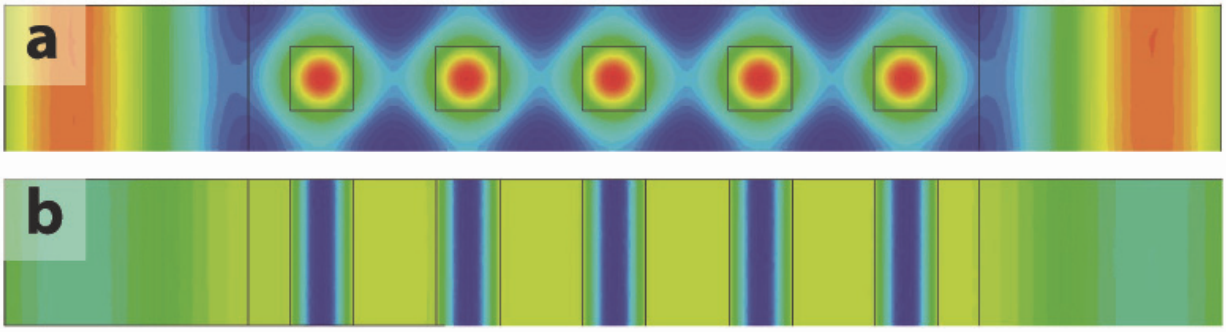

Figure S5 Simulated field profile across the ZIM. Simulated **a,** E_x and **b,** H_y field plots on the *y-z* and *x-z* planes, respectively at Dirac point frequency. Each unit cell resonates in phase with one another and no net spatial phase change occurs.

g. Comparison of spontaneous emission from emitters embedded in air and ZIM media.

The strength of spontaneous emission from emitters embedded inside a ZIM or very low index material depends on two important factors: (1) the optical density of states available to the emitters and (2) constructive interference of the emitters. To better illustrate these effects we have simulated the emission of a single and multiple emitters in a homogeneous slab of material with $n = 0.01$ and compared it to the identical cases in air. For the single emitter case, there is no constructive interference and due to the lower density of states available to the emitter, the emission is low. This can be observed in the single emitter case in Fig. S6(a,b), where intensity in the normal direction is roughly 1.5X less than in air and the total emitted intensity is ~50X less than in the air case. However, as we add more emitters to the ZIM, the emission interferes constructively. In the case of 10 emitters, the emission intensity in the direction normal to the slab increases by 100X, or with the square of the number of emitters added, due to constructive interference. The intensity of light emission normal to the surface is now higher in the ZIM case but the integrated total emission remains 10X smaller than the air case. Constructive interference

is in fact one of the most significant benefits of having a zero-index material as it allows one to realize relatively coherent emission from incoherent sources. In all the simulations the emitters are oscillating with the same phase and have random positions within the material, leading to a non-uniform profile in air. As such, we have provided an isotropic, averaged, emission profile that corresponds to the total emitted power in the air case for better visualization (purple dashed line).

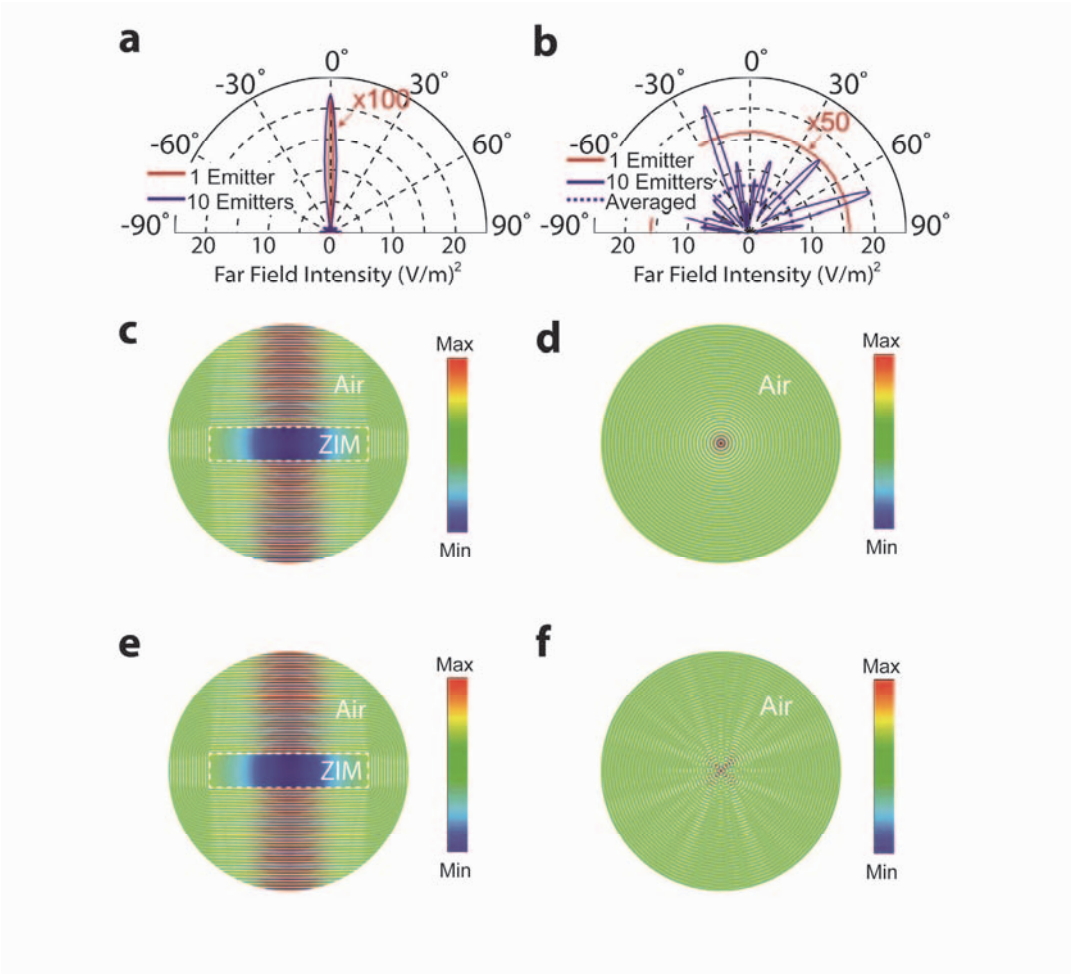

Figure S6 Emission profiles for single and multiple emitters in a ZIM and air. a, Emission profiles in a ZIM, **b,** emission profiles in air, the blue dashed line represents an averaged emission intensity for all angles for the 10 emitters case.. **c-d,** Electric field plots for single emitters in a ZIM and air, respectively. **e-f,** Electric field plots for 10 emitters in a ZIM and air, respectively.

DOI: 10.1038/NPHOTON.2013.214

S2. Fabrication

We developed a unique low pressure chemical vapor deposition (LPCVD) process to deposit 11 alternating layers of α-Si (260 nm) and SiO_2 (340 nm) during a single process run on a 4 inch quartz wafer. The LPCVD tool used was a horizontal tube furnace. A quartz caged boat was used to contain the wafer to improve cross wafer uniformity. Deposition temperature was 550°C and process pressure was 300mTorr and both were held constant throughout the deposition of both films. Process gases were introduced into the tube furnace via mass flow controllers. The α-Si layer was deposited by flowing 50sccm's of 100% SiH_4. The SiO_2 layer was deposited by flowing 85sccm's of SiH_4 and 120sccm's of O_2. A brief N_2 purge was introduced between layers. This alternating process was repeated until the desired number of layers was deposited.

A hard metal etch mask was patterned using electron beam lithography (Raith and/or Jeol) and deposition of 50 nm chromium (Cr) followed by lift-off. To avoid surface charging detrimental effects, electron beam sensitive resist (ZEP520A and/or PMMA) was coated with a 10 nm Cr charge dissipation layer to be chemically removed prior to the exposed resist development. A fluorine based reactive ion etching (RIE) recipe was developed in an Oxford Plasma Lab tool to etch the multilayer sample by alternating the recipe for the Si and SiO_2 layers. The final structure has a 10:1 aspect ratio with respect to the total height and gap width between the rods. The base etch recipe involved 100 W RF power, 2000 W ICP power with C_4F_8 and O_2 gas flows for the SiO_2 layers and 80 W RF, 1200 W ICP with C_4F_8, SF_6, O_2 and Ar gas flows for the α-Si layers. The oxide had a positive slope as we etched down to subsequent layers underneath. Starting with the base recipe for the upper layers, the subsequent SiO_2 layers were etched more aggressively with increasing depth. This was accomplished by changing the ratio of C_4F_8 and O_2 gas-flow which provided less passivation to the side walls during etching. The base Si etch recipe resulted in straight side walls until we reached the bottom most layer. The bottom

most oxide and Si layers were etched with the most aggressive recipes and the top layers were protected by additional passivation steps. The metamaterial's internal structure was characterized by imaging the edge profile after milling cross-sections inside the array using focused ion beam milling (FIB). During all imaging, a thin layer of Cr was deposited on the sample to provide a conducting surface.

We made sure that PMMA, which was spin-coated on the sample after the RIE process, filled in the gaps completely in order to provide a background with the same permittivity as the SiO_2 spacer layers. The sample with a drop casted PMMA film was placed in an evacuated desiccator to remove air bubbles and this process was followed by spinning and soft baking (120 degrees for 2 minutes) twice and reflowing at 300˚ C for 2 minutes to reach the desired thickness. The final structure was cross-sectioned with FIB milling at multiple locations to confirm the complete filling.

S3. Characterization

To experimentally verify the ability to modify spontaneous emission, we placed quantum dots (QDs) within the ZIM and compared their emission profile with PMMA/QD composites spun onto a bare quartz substrate. To place the QDs within the ZIM, we sandwiched the QD film between two PMMA layers by drop casting 10 μL of PbS QDs in toluene and baking it at 60 °C for 10 minutes. The quantum dots were purchased from Evident Technology and have an average diameter of 4.6 nm with oleic acid as the capping ligand. The quantum dots were incorporated in a thin layer within the metamaterial by first spinning a thin PMMA film, filling the structure half-way, and then spinning the quantum dots (in toluene) in a thin layer. A second PMMA film was then spun to fill up the entire structure. The QD-embedded ZIM was excited by a tightly-focused 1064 nm laser beam, and the emission spectrum (Fig. S7) and Fourier plane

DOI: 10.1038/NPHOTON.2013.214

image were collected at the transmission side, with a 1200 nm long pass filter and a polarizer placed behind the sample.

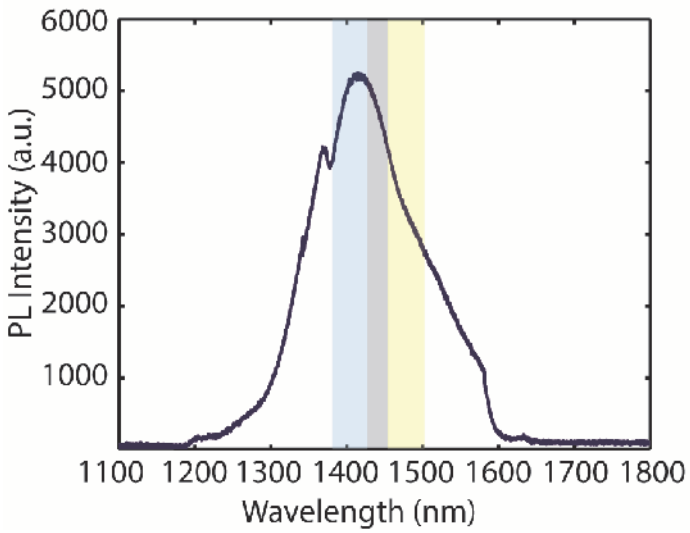

Figure S7 QD Emission Spectrum. Photoluminescence (PL) spectrum of PbS quantum dots (Evident Technology) used in the main text. The emission peak appears at 1425 nm, with a full-width at half-maximum of 172 nm. The blue-, gray- and yellow-shaded region corresponds to positive index, metallic properties, and negative index as acquired from S-parameter retrieval. The dip of measured luminescence spectrum at around 1380 nm is due to the water absorption line.

References

1. Foteinopoulou1, S. & Soukoulis, C. M. Electromagnetic wave propagation in two-dimensional photonic crystals: A study of anomalous refractive effects. *Phys. Rev. B* **72**, 165112, (2005).

2. Wu, Y., Li, J., Zhang, Z.-Q. & Chan, C. Effective medium theory for magnetodielectric composites: Beyond the long-wavelength limit. *Phys. Rev. B* **74**, (2006).

CST视频培训课程推荐

CST 微波工作室(CST Microwave Studio)是 CST 工作室套装中最核心的一个子软件，主要用于三维电磁问题的仿真分析，可计算任意结构任意材料电大宽带的电磁问题。广泛应用于高频/微波无源器件的仿真设计、各种类型的天线设计、雷达散射截面分析、电磁兼容分析和信号完整性分析等各个方面。

易迪拓培训(www.edatop.com)推出的 CST 微波工作室视频培训课程由经验丰富的专家授课，旨在帮助用户能够快速地学习掌握 CST 微波工作室的各项功能、使用操作和工程应用。购买 CST 教学视频培训课程套装，还可超值赠送 3 个月免费在线学习答疑，让您学习无忧。

CST 学习培训课程套装

该培训套装由易迪拓培训联合微波 EDA 网共同推出，是最全面、系统、专业的 CST 微波工作室培训课程套装，所有课程都由经验丰富的专家授课，视频教学，可以帮助您从零开始，全面系统地学习 CST 微波工作的各项功能及其在微波射频、天线设计等领域的设计应用。且购买该套装，还可超值赠送 3 个月免费学习答疑…

课程网址：http://www.edatop.com/peixun/cst/24.html

HFSS 天线设计培训课程套装

套装共含 5 门视频培训课程，课程从基础讲起，内容由浅入深，理论介绍和实际操作讲解相结合，全面系统的讲解了 CST 微波工作室天线设计的全过程。是国内最全面、最专业的 CST 天线设计课程，可以帮助您快速学习掌握如何使用 CST 设计天线，让天线设计不再难…

课程网址：http://www.edatop.com/peixun/cst/127.html

更多 CST 视频培训课程：

- **CST 微波工作室入门与应用详解 — 中文视频教程**
  CST 微波工作室初学者的最佳培训课程，由工程经验丰富的资深专家授课，全程中文讲解，高清视频，直观易学。网址：http://www.edatop.com/peixun/cst/25.html
- **CST 微波工作室天线设计详解 — 中文视频培训教程**
  重点讲解天线设计相关知识和使用 CST 进行天线仿真设计的使用操作，是学习掌握使用 CST 微波工作室进行天线设计的必备课程，网址：http://www.edatop.com/peixun/cst/26.html
- **CST 阵列天线仿真设计实例详解 —— 中文视频教程**
  阵列天线设计专业性要求很高，因此相关培训课程是少之又少，该门培训课程由易迪拓培训重金聘请专家讲解；课程网址：http://www.edatop.com/peixun/cst/123.html
- **更多 CST 培训课程**，敬请浏览：http://www.edatop.com/peixun/cst

关于易迪拓培训：

易迪拓培训(www.edatop.com)由数名来自于研发第一线的资深工程师发起成立，一直致力和专注于微波、射频、天线设计研发人才的培养；后于 2006 年整合合并微波 EDA 网(www.mweda.com)，现已发展成为国内最大的微波射频和天线设计人才培养基地，成功推出多套微波射频以及天线设计相关培训课程和 ADS、HFSS 等专业软件使用培训课程，广受客户好评；并先后与人民邮电出版社、电子工业出版社合作出版了多本专业图书，帮助数万名工程师提升了专业技术能力。客户遍布中兴通讯、研通高频、埃威航电、国人通信等多家国内知名公司，以及台湾工业技术研究院、永业科技、全一电子等多家台湾地区企业。

我们的课程优势：

※ 成立于 2004 年，10 多年丰富的行业经验

※ 一直专注于微波射频和天线设计工程师的培养，更了解该行业对人才的要求

※ 视频课程、既能达到现场培训的效果，又能免除您舟车劳顿的辛苦，学习工作两不误

※ 经验丰富的一线资深工程师讲授，结合实际工程案例，直观、实用、易学

联系我们：

※ 易迪拓培训官网：http://www.edatop.com

※ 微波 EDA 网：http://www.mweda.com

※ 官方淘宝店：http://shop36920890.taobao.com